11th World Congress on Computational Mechanics (WCCM XI)
5th European Conference on Computational Mechanics (ECCM V)
6th European Conference on Computational Fluid Dynamics (ECFD VI)
E. Oñate, J. Oliver and A. Huerta (Eds)

ON THE ESTIMATION OF SPANWISE PRESSURE COHERENCE OF A TURBULENT BOUNDARY LAYER OVER A FLAT PLATE

W.C.P. VAN DER VELDEN*, A.H. VAN ZUIJLEN*, A.T. DE JONG* AND H. BIJL*

* Aerodynamics Department, Faculty of Aerospace Engineering
Delft University of Technology
Kluyverweg 2, 2629HT Delft, the Netherlands
e-mail: W.C.P.vanderVelden@TUDelft.nl

Key words: Computational Aero-Acoustics, Computational Fluid Dynamics, Large Eddy Simulation

Abstract. A Large Eddy Simulation (LES) with four different closure models are analyzed in OpenFOAM, an open source Computional Fluid Dynamics (CFD) package and validated for the determination of the streamwise and spanwise coherence length of the pressure field below a turbulent boundary layer at low Reynolds numbers. Matching results are found for outer scaling mean and fluctuating velocity data as well as for the pressure spectrum data. The coherence function shows a similar decay with respect to various literature studies. An exponential fit is applied to determine the coherence length. Agreement within one displacement thickness error in streamwise and spanwise direction is found for the coherence length with semi-empirical data. The spanwise coherence length is considerably smaller than the streamwise coherence length, but indicates a clear peak in the low frequency regime originating from large coherent structures with relatively small amplitudes.

1 INTRODUCTION

Far field noise pollution is one of the main design drivers for, for example on-shore wind energy. The turbulent trailing edge noise of a wind turbine blade is currently one of the most dominant noise sources on a wind turbine and therefore understanding the physics associated with the generation and propagation is of main importance for the design of more silent wind turbines. Regarding hybrid aeroacoustic methods, pressure and velocity fluctuations are the main quantities of interest for determining the acoustic sources. Especially the spanwise coherence of the wall pressure is of importance for the estimation of, for example, trailing edge noise and vibro-structural problems. Several authors,

such as Amiet [1] and Howe [2] have discussed difraction theory regarding trailing edge noise. Here, the power spectral density and spanwise coherence length of hydrodynamic pressure fluctuations were used to estimate the acoustic far field spectrum. Amiet [1] and Howe [2] assumed that the incident pressure fluctuations on the wall below the turbulent boundary convect over the trailing edge, which acts as an impedance discontinuity, where the fluctuations are scattered in the form of acoustical waves. This theory forms the basis of multiple experimental and numerical studies, such as the LES study of Christophe [3] or the surface pressure measurements of Brooks and Hodgson [4].

This study focuses on the very first part of capturing trailing edge noise; the physically correct simulation of a turbulent boundary layer of low Mach number flow. Particularly, the spanwise coherence length of the hydrodynamic pressure fluctuations is investigated. When the methodology proposed in next section is shown to be successful the study will be extended to a finite flat plate, simulating trailing edge noise.

Numerical data will be obtained from a Large Eddy Simulation (LES) using the open-source package OpenFOAM in combination with four sub-grid scale closure models. A Direct Numerical Simulation (DNS) and Particle Image Velocitimetry (PIV) reference study of Pröbsting et al. [5] is used to compare the results found.

2 METHODOLOGY

2.1 Governing fluid equations

Since a low Mach number flow over an infinite flat plate is considered, the incompressible Navier-Stokes equations are used to describe the fluid dynamics. Further, Newtonian fluid properties are assumed and gravity forces and other body forces are neglected, resulting in the following simplified set of equations, describing the conservation of mass and momentum:

$$\nabla \cdot \mathbf{u} = 0, \tag{1}$$

$$\frac{\partial \mathbf{u}}{\partial t} + \nabla \cdot (\mathbf{u}\mathbf{u}) = -\frac{\nabla p}{\rho} + \nabla \cdot (\nu \nabla \mathbf{u}), \tag{2}$$

wherein $\mathbf{u}$ are the different velocity components, p is the pressure, ρ the density and ν the kinematic viscosity.

A LES methodology is applied, resolving all large eddy scales, while smaller eddy scales are modeled. This methodology is known as the balanced form between completely modeling the turbulence (Reynolds Averaged Navier-Stokes, RANS) and completely solving the turbulence (Direct Numerical Simulation, DNS).

Discretization of the first time derivative is performed via a second order backward difference scheme. The velocity and pressure gradient are discretized using a second order, Gaussian linear interpolation (central differencing), while the velocity divergence is interpolated using a second order, Gaussian linear interpolation with filtering for high-frequency ringing. Finally the Laplacian of the kinematic viscosity and the velocity is discretized using the second order, Gaussian unbounded, second order, conservative scheme.

The discretized set of equation is solved in the open-source package OpenFOAM, based on the Finite Volume Method (FVM) [6]. The large time-step transient solver for incompressible flow, pimpleFoam, is used using the PIMPLE (merged PISO-PIMPLE) algorithm. PISO is an acronym for Pressure Implicit Splitting of Operators for time dependent flows while SIMPLE stands for Semi-Implicit Method for Pressure Linked Equations which is used for steady state problems. The PISO algorithm neglects the velocity correction in the first step, but then performs one in a later stage, which leads to additional correction for the pressure [7].

2.2 Sub grid scale models

Four different Sub Grid Scale (SGS) models, used for determining the eddy viscosity, are validated and compared; the homogeneous dynamic Smagorinsky model, the selective Smagorinsky model, the Spalart-Allmaras Improved Delayed Detached Eddy Simulation (IDDES) and an implicit model, thus avoiding a SGS model.

The homogeneous dynamic Smagorinsky model is an algebraic eddy viscosity SGS model founded on the assumption that local equilibrium prevails. In the dynamic version, the two coefficients are calculated during the simulation. The averaging is performed over the whole domain, i.e. homogeneous turbulence is assumed [6]. The selective Smagorinsky model on the other hand, is a local method validated specifically for wall bounded flows which is derived by Sagaut [8]. The SGS model is a combination of the basic Smagorinsky model together with a selection function, which will be locally turned on and off on a specific value of the local angular fluctuations of the instantaneous vorticity. The third model involves a DES, a blending between the statistical RANS model and the LES model. The method is developed to overcome excessive computer demands of LES. The basic principle is to solve the boundary layer with RANS, whereas LES is used for the external flow and separation regions. The IDDES is an improved model, to overcome problems with the transition from RANS to LES [9]. An alternative to these explicit methods is the Implicit LES (ILES), where numerical schemes are used such that the inviscid energy cascade through the inertial range is captured accurately and the inherent numerical dissipation emulates the effect of the dynamics beyond the grid-scale cut-off [10].

2.3 Recycling method

To simulate a LES on a infinite flat plate within current computational demands, a recycling method is used. The main idea behind the recycling and rescaling inflow modeling approach is to extract data at a station downstream from the inflow, and rescale it to account for boundary layer growth. In the approach by Lund [11], the flow at the extraction station is averaged in spanwise direction and in time, to allow the decomposition of the flow field in a mean and fluctuating part. The mean velocities and fluctuations are then rescaled according to the law of the wall in the inner region and the defect law in

the outer region, and blended together using a weighted average of the inner and outer profiles:

$$\begin{aligned}(u_i)_{in} &= \left\{(U_i)_{in}^{inner} + (u_i')_{in}^{inner}\right\}\left[1 - W(\eta_{in})\right] \\ &+ \left\{(U_i)_{in}^{outer} + (u_i')_{in}^{outer}\right\}\left[W(\eta_{in})\right], \end{aligned} \tag{3}$$

with the weighting function defined as:

$$W(\eta) = \frac{1}{2}\left\{1 + \frac{1}{\tanh(\alpha)}\tanh\left[\frac{\alpha(\eta - b)}{(1-2b)\eta + b}\right]\right\}, \tag{4}$$

wherein $\eta = y/\delta$ indicates the outer coordinate scaling and $\alpha = 4$ and $b = 0.2$ are prescribed constants [11]. Interpolation is linear.

2.4 Definition and estimation of coherence

For determination of the coherence length, first the coherence function should be evaluated. The coherence function is the auto-power and cross-power density of the signals, where $\Phi(\omega, z_1, z_2)$ denotes the cross-power spectral density between two points along a given dimensional line $\Delta z = z_2 - z_1$, with ω defined as the angular frequency:

$$\gamma^2(\omega, \Delta z) = \frac{\left|\Phi(\omega, z_1, z_2)\right|^2}{\left|\Phi(\omega, z_1, z_1)\right|\left|\Phi(\omega, z_2, z_2)\right|}. \tag{5}$$

This representation is valid for the case that the flow statistics are homogeneously distributed along the spatial dimension, stationary in time and for an infinite observation period. For a flat plate the first criteria is fulfilled when considering the spanwise direction, and with restriction to very short separations, also for the streamwise direction. By definition, the coherence length is related to the integral of coherence function over the spatial separation Δz and therefore reduces to a function of frequency only:

$$l_z(\omega) = \lim_{L\to\infty}\int_0^L \gamma(\omega, \Delta z)\, d\Delta z. \tag{6}$$

This relation can be used to obtain the coherence length. However, due to convergence issues, first observed by Christophe [3] for his LES data with a finite observation period, the coherence does not approach zero for very large separations Δz and therefore, the integral might be unbounded. Instead, in this study a curve fitting approach based on an exponential function is applied ([12]):

$$\gamma(\omega, \Delta z) = e^{-\frac{|\Delta z|}{l_z(\omega)}}. \tag{7}$$

The fit is performed for each discrete frequency and has shown to be a robust alternative to Eq. 6.

3 MODEL SET-UP

The current study investigates a turbulent boundary layer on a flat plate of 400 mm chord, with a wetted span of 40 mm (Fig. 1). The measurement volume in wall-normal direction equals 30 mm. Reference length and velocity scales are the boundary layer thickness and the free stream velocity at 250 mm downstream at the center of the computational domain. At a free stream velocity of $u_\infty = 10$ m/s the Reynolds number based on the local boundary layer thickness $\delta = 10.4$ mm is $Re_\delta \approx 6,800$ and based on the momentum thickness $\theta = 1.1$ mm is $Re_\theta \approx 750$. A complete overview of all model parameters can be found in Tab. 1, including a comparison with the reference data of Pröbsting [5].

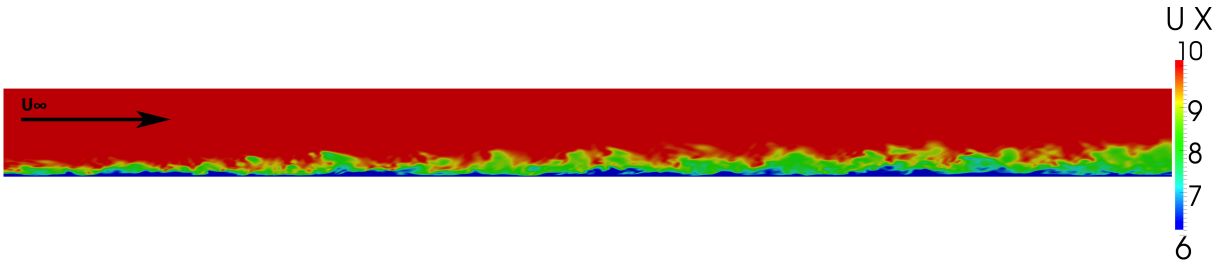

Figure 1: Snapshot at $t = 0.5$ s of streamwise velocity over the plate

The domain is discretized in $800 \times 100 \times 80$ cells, resulting in vector sampling of $\Delta x/\delta \approx 0.048$ and $\Delta z/\delta \approx 0.048$ in streamwise and spanwise direction respectively. In wall-normal direction the sampling resolution ranges from $\Delta y/\delta \approx 0.004$ near the wall to $\Delta y/\delta \approx 0.1$ in the free stream. An adjustable time step is used, keeping the Courant number below one. In practice this yields steps of $\Delta t \approx 2 \cdot 10^{-5}$. Pressure and velocity fluctuations are stored each 4 steps, which results in a temporal sampling of $\Delta t u_\infty/\delta \approx 0.07$ ($\omega\delta^\star/u_\infty \approx 13.3$). For the present study, approximately $4,000$ samples equivalent to a non-dimensional time interval of $Tu_\infty/\delta \approx 300$.

As discussed, a recycle inflow flow condition is used for turbulent boundary layer growth. At the outlet and top of the model, velocity is imposed by a Neumann boundary condition. The wall is modeled with a no-slip condition. Both sides of the domain are cyclic, to simulate an infinite span. Regarding pressure boundary conditions, the top boundary is set to outside atmospheric pressure, while all other boundaries are modeled using the Neumann condition.

4 RESULTS

4.1 Mean velocity and Reynolds stresses

An overview of the boundary layer growth along the plate is illustrated in Fig. 1. At 250 mm downstream, measurements were taken for this study. All parameters, extracted from the LES simulation are summarized in Tab. 1. Please note that these are averaged

Table 1: Boundary layer parameters from current study and comparison study from Pröbsting [5]

Parameter	**Symbol**	**LES**	**PIV**	**DNS**
Boundary layer thickness [mm]	δ	10.4	9.4	9.4
Displacement thickness [-]	$\delta^\star/\delta$	0.16	0.16	0.18
Momentum thickness [-]	θ/δ	0.11	0.12	0.12
Wall shear velocity thickness [-]	u_τ/u_∞	0.045	0.052	0.053
Shape factor [-]	H	1.48	1.45	1.50
Reynolds number [-]	Re_δ	6,800	6,240	8,185
	Re_θ	750	730	1,000
	Re_τ	310	436	325

parameters for all four models, although the differences between the SGS models are found to be negligible.

The mean velocity profiles for the four different LES models scaled with outer scaling variables are displayed in Fig. 2. A 2% difference is found for all simulations and comparison data. A shape factor of $H = \delta^\star/\theta = 1.48$ is found, which confirms the presence of a fully developed turbulent boundary layer.

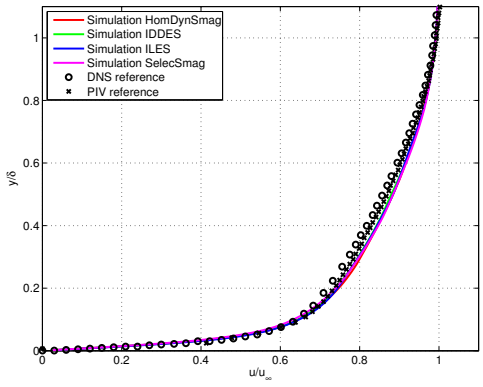

Figure 2: Mean velocity in outer scaling

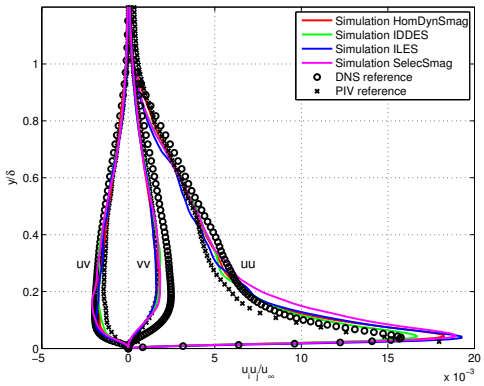

Figure 3: Reynolds stress profiles in outer scaling

The distributions of the Reynolds stress tensor are attached in Fig. 3. All models show excellent agreement (within 95% accuracy) with each other and with the reference results. When approaching the wall, the streamwise velocity fluctuations measured with IDDES underestimate all other LES models. This is a result of the averaging effect due to the RANS approach near the wall. The other two normal components of the Reynolds stress tensor show similar patterns.

As an indication for the outer time scale the eddy turn over time is estimated with $\delta/u_\infty \approx 1$ ms or a non-dimensional frequency of $\omega\delta^\star/u_\infty \approx 1$. In non-dimensional units, this results in $\omega\delta^\star/u_\infty \approx 14.5$. Since the temporal sampling of the LES was set at

$\omega\delta^\star/u_\infty \approx 13.3$, it is sufficient to sample the outer time scale. In the remainder of this study, $\delta^\star/u_\infty$ and $\delta^\star$ are used as outer time and length scale respectively.

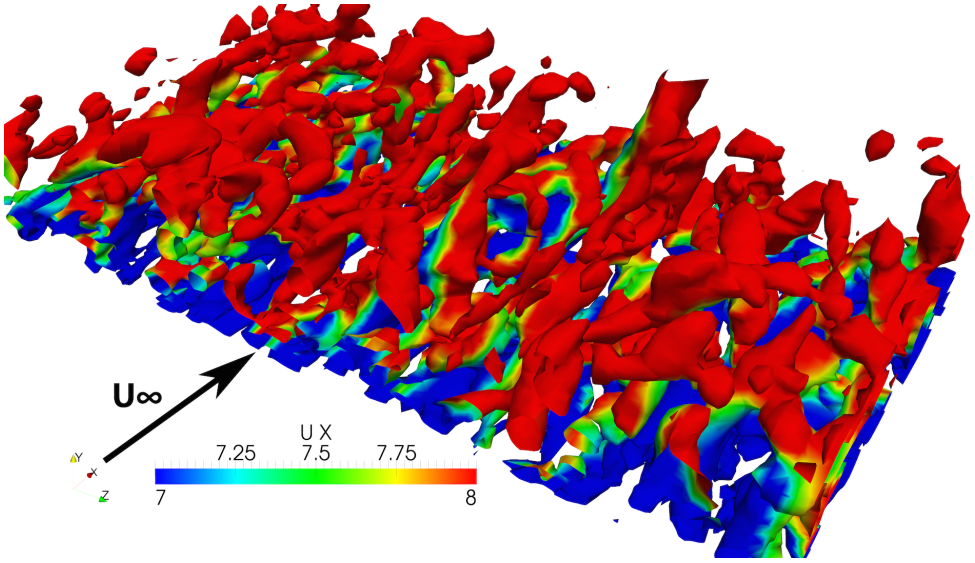

Figure 4: Instantaneous visualization of second invariant of the velocity gradient tensor iso-contours ($Q = 0.2 \cdot 10^6$), colored by the streamwise velocity

4.2 Velocity spectrum and coherence

The unsteady organization and evolution of coherent structures within the turbulent boundary layer is further investigated using Fig. 4, where the second invariant of the velocity gradient tensor (Q) is plotted. The interaction between the low-speed streaks (blue) and vortical structures (red) are shown by means of hairpin packets, full fairpins, legs and cane vortices [13].

Next, the spectral energy distribution and the coherence are examined for the streamwise and wall-normal velocity components. Data is sampled at a probe located at $y/\delta = 0.1$ and converted to a Power Spectral Density (PSD) signal using Welch's method, together with a Hanning window of 128 samples with 50 % overlap [14]. The result is depicted in Fig. 5. Clearly, the streamwise velocity fluctuations show a higher energy content at lower frequency. This is caused by the streamwise coherent regions of low speed fluid originating from the viscous sublayer convected into the upper regions of the boundary layer. On the other hand, wall-normal velocity fluctuations are associated with ejection and sweep events of much smaller extent [5, 15]. Both velocity fluctuation spectra start to coincide at $\omega\delta^\star/u_\infty = 1.5$ and start following a decay of approximately ω^{-5}.

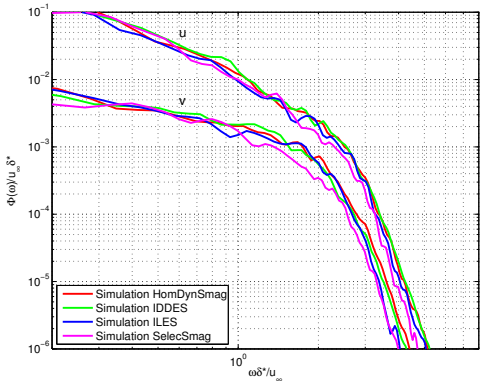

Figure 5: Normalized power spectral density of the streamwise and wall-normal velocity fluctuations at $y/\delta \approx 0.1$

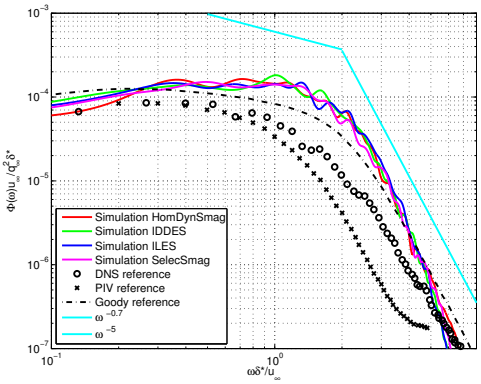

Figure 6: Pressure spectrum scaled with outer variables

4.3 Wall pressure fluctuations and spectrum

The pressure fluctuations, resulting from the streamwise and wall-normal velocity fluctuations, are further discussed. A probe is located in the middle of the plate and sampled the pressure fluctuations on the wall. The signal is transferred to a PSD using the same procedure as described in previous section and plotted in Fig. 6. PIV and DNS references are attached, as well as an estimation of the spectrum provided by the model of Goody [16]. Again, the internal comparison between all LES models does not give any conclusions about the most suitable model to predict pressure fluctuations. At the mid frequencies, the LES overestimates the PSD compared to the analytical result with $1-3$ dB. When $\omega\delta^\star/u_\infty \geq 2$ the LES follows the decay of the reference, theoretical and analytical model of ω^{-5}. The indicated slope of $\omega^{-0.7}$ is characteristic for the overlap region, which becomes narrow for very low Reynolds numbers [16].

4.4 Wall pressure coherence

To determine wall pressure coherence, the pressure in streamwise and spanwise direction are sampled along a line. With these data, Eq. 5 can be solved in both directions. The results are found in Fig. 7 & 8. In general, the coherence along the streamwise direction attains much higher values at low frequencies and decays beyond the resolvable scales at higher frequencies $\omega\delta^\star/u_\infty \geq 4.5$. At high frequencies, large coherence is present for the LES homogeneous Dynamic Smagorinsky model. Also the selective Smagorinsky model shows a minor increase at the high frequency range. It is unknown why this sudden increase happens. Nevertheless the decay of the coherence function until $\omega\delta^\star/u_\infty \leq 2.5$ is similar in all cases, as well with the comparison study of Pröbsting [5], depicted in Fig. 9.

The spanwise coherence estimate, depicted in Fig. 8, only shows some coherence at low frequencies. A larger discrepancy is found when comparing each LES model. Especially

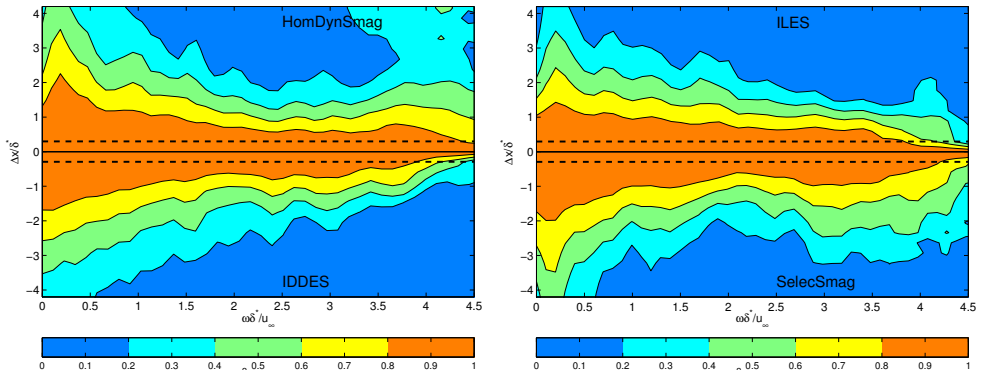

Figure 7: Streamwise coherence function $\gamma_p^2(\omega, \Delta x)$ of pressure fluctuations on the wall

the homogeneous Dynamic Smagorinsky model differs; it captures more coherence at lower (but not the lowest) frequencies. When $\omega\delta^\star/u_\infty \geq 2$ the coherence falls within the resolution of the LES (i.e. $\Delta z/\delta^\star = 0.5/1.7 \approx 0.29$). This region barely shows any dependence on the frequency.

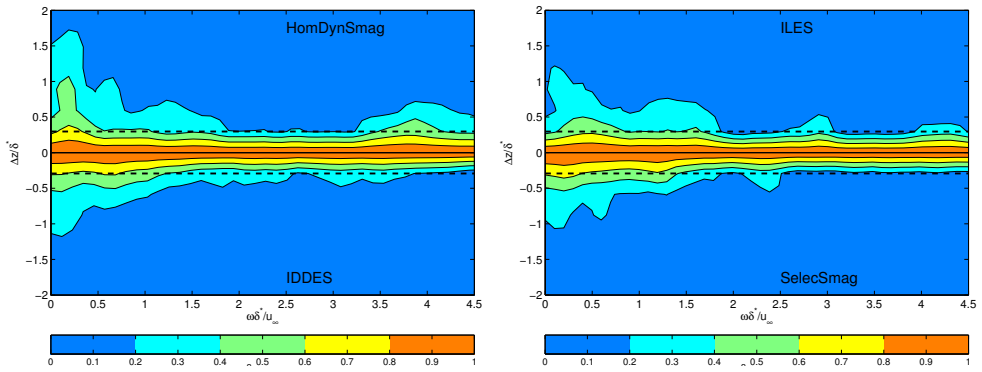

Figure 8: Spanwise coherence function $\gamma_p^2(\omega, \Delta z)$ of pressure fluctuations on the wall

The coherence of pressure fluctuations over the span show a substantially faster decay compared to the streamwise direction, indicating that the resolution of the simulation is a key parameter. Therefore, an implicit LES model with finer spanwise resolution ($\Delta z/\delta \approx 0.024$) is run and compared with the standard mesh ($\Delta z/\delta \approx 0.048$). Results of the pressure coherence function in spanwise direction is attached in Fig. 10. Clearly, decreasing the cell size increases the coherence at all frequencies. Coherent structures at a single broad frequency band are now discovered within the resolution of the simulation, which was also seen in the reference DNS results from Fig. 9.

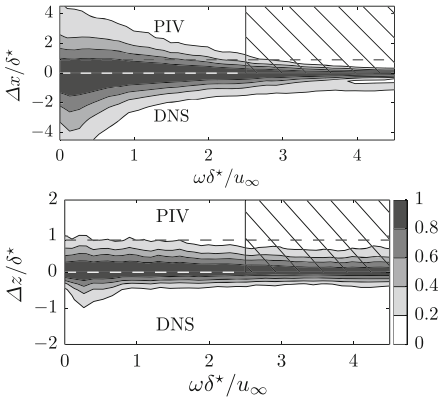

Figure 9: Streamwise and Spanwise coherence function from Pröbsting et al.[5]

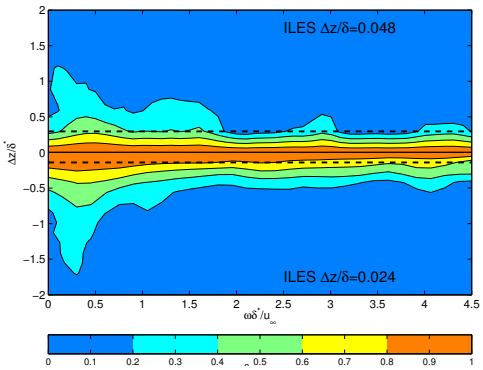

Figure 10: Comparing mesh density for spanwise coherence function $\gamma_p^2(\omega, \Delta z)$ of pressure fluctuations on the wall

4.5 Coherence length

The final estimation of the coherence length involves the integration of the coherence function. However, since this led to convergence issues in the past, instead an exponential fit based solution is applied [3]. The fitting has been applied to all the data points in the region $0 \leq \Delta x/\delta^\star \leq 4$. Clearly, from previous contours, the spanwise coherence length is marginally compared with the streamwise coherence length. For each discrete frequency, this exponential fit approach is applied. This results in streamwise and spanwise coherence lengths depicted in Fig. 11 & 12. Comparing both figures, indeed the streamwise coherence length is considerably larger than the spanwise coherence length, especially for low frequencies. As a comparison, the PIV and DNS results can be used. A close correspondence is found at all frequencies with the DNS data of Pröbsting et al. [5]. Also the empirical model of Corcos [17] is attached for comparison. The streamwise coherence estimate from Corcos [17] start to match at $\omega\delta^\star/u_\infty \approx 1.0$ and start showing a similar decay. Only the homogeneous Dynamics Smagorinsky and selective Smagorinsky start to deviate from this empirical solution by a sudden increase in coherence length at high frequencies. These discrepancies are not fully understood yet and require further attention. In addition, at frequencies $\omega\delta^\star/u_\infty \geq 4.0$, this behavior was also found at the DNS simulation of Pröbsting [5].

The spanwise coherence result in Fig. 12 also match with the decay and values of the empirical model of Corcos [17] in the higher frequency regions. In the lower frequency regions, the error does not exceed one displacment thickness error. Note that the coherence length estimate is only a small fraction of the displacement thickness $\delta^\star$, which implies very small structures of very small amplitudes. Therefore, at low frequencies, the decrease in spanwise cell size enables better capturing of these structures. A larger coherence length is found comparing both ILES simulations.

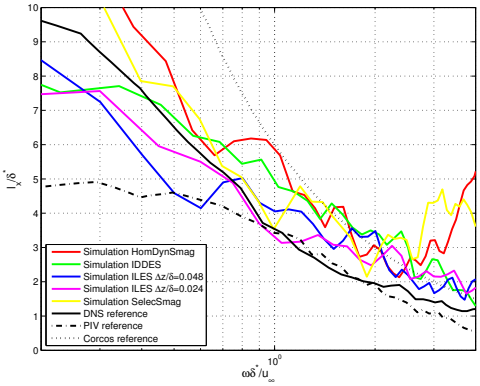

Figure 11: Streamwise coherence length

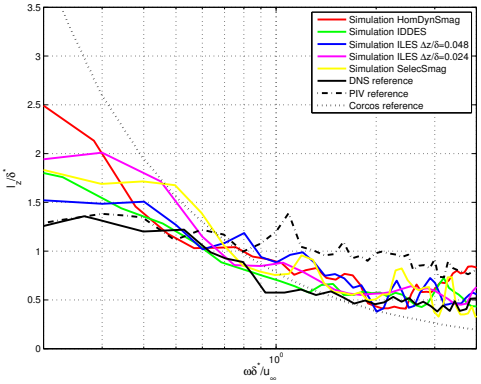

Figure 12: Spanwise coherence length

5 CONCLUSION

The current study deals with the estimation of the streamwise and spanwise coherence length of the pressure field below a turbulent boundary layer at low Reynolds numbers using four different LES closure models implemented in OpenFOAM, an open source CFD software package. Results have been compared to DNS and PIV results from Pröbsting et al. [5], as well as empirical models from Goody [16] and Corcos [17].

Results for outer scaling mean and fluctuating velocity data matches the PIV and DNS reference data within 95 % accuracy. The pressure spectrum agrees well with the reference results. Only a small overestimation at mid frequency range is observed. The decay at larger frequencies corresponds to the theoretical decay of ω^{-5}.

Regarding the streamwise coherence, the decay as well as the values are similar to the PIV and DNS results. In constrast, the spanwise coherence is limited by its small length and strength relatively to the mesh resolution. Increasing the spanwise mesh resolution enables capturing large coherent structures at low frequencies.

For the estimation of the coherence length, an exponential fit based solution is applied. Results of all four closure models match the decay of the reference result from Corcoc [17] from $\omega\delta^\star/u_\infty \geq 1.0$ and onwards, while the DNS results are almost identical to all results. The spanwise coherence length is significantly smaller than the streamwise coherence length, indicating low amplitude structures.

In conclusion, all models are applicable for further aeroacoustic analysis. Further analysis with respect to trailing edge flow is required to select the most suitable simulation. Regarding computational time, the ILES as well as the selective Smagorinsky model show a 20 % reduction with respect to the homogeneous Smagorinksy model, making these two models good candidates for further analysis.

ACKNOWLEDGMENTS

This research is funded and supported by Siemens Wind Power A/S, Brande, Denmark.

References

[1] Amiet, R. Noise due to turbulent flow past a trailing edge. *Journal of Sound and Vibration*, (1976), **47**(3):387–393.

[2] Howe, M. Trailing edge noise at low mach numbers. *Journal of Sound and Vibration*, (1999), **225**(2):211–238.

[3] Christophe, J. *Application of hybrid methods to high frequency aeroacoustics*. PhD thesis, Université Libre de Bruxelles, (2011).

[4] Brooks, T. and Hodgson, T. Trailing edge noise prediction from measured surface pressures. *Journal of Sound and Vibration*, (1981), **78**(1):69–117.

[5] Pröbsting, S., Scarano, F., Bernardini, M., and Pirozzoli, S. On the estimation of wall pressure coherence using time-resolved tomographic piv. *Experimental Fluids*, (2013), **54**:1567–1582.

[6] OpenFOAM. *OpenFOAM: The Open Source CFD Toolbox Programmer's Guide*. ESI-Group, (2012).

[7] Issa, R. Solution of the implicitly discretised fluid flow equations by operator-splitting. *Journal of Computational Physics*, (1986), **62**:40–65.

[8] Sagaut, P., Montreuil, E., and Labbé, O. Assessment of some self-adaptive sgs models for wall bounded flows. *Aerospace Science and Technology*, (1999), **6**:335–344.

[9] Shur, M., Spalart, P., Strelets, M., and Travin, A. A hybrid rans-les approach with delayed-des and wall-modelled les capabilities. *International Journal of Heat and Fluid Fluid*, (2008), **29**(6):1638–1649.

[10] Boris, J. New insights into large eddy simulation. *Fluid Dynamics Research*, (1992), **10**:199–229.

[11] Lund, T., Wu, X., and Squires, K. Generation of turbulent inflow data for spatially-developing boundary layer simulations. *International Journal of Computational Physics*, (1998), **140**(2):233–258.

[12] Palumbo, D. Determining correlation and coherence lengths in turbulent boundary layer flight data. *Journal of Sound and Vibration*, (2012), **331**(16):3721–3737.

[13] Ghaemi, S. and Scarano, F. Counter-hairpin vortices in the turbulent wake of a sharp trailing edge. *Journal of Fluid Mechanics*, (2011), **689**:317–356.

[14] Welch, P. The use of fast fourier transform for the estimation of power spectra; a method based on time averaging over short modified periodograms. *IEEE Trans Audo Electroacoustics*, (1967), **15**(2):70–73.

[15] Robinson, S. Coherent motions in the turbulent boundary layer. *Annual Review of Fluid Mechanics*, (1991), **23**(1):601–639.

[16] Goody, M. Empirical spectral model of surface pressure fluctuations. *AIAA Journal*, (2004), **42**(9):1788–1794.

[17] Corcos, G. The structure of the turbulent pressure field in boundary layer flows. *Journal of Fluid Mechanics*, (1964), **18**(3):353–378.